Journal of Sensor Science and Technology
Vol. 32, No. 6 (2023) pp. 340-351
http://dx.doi.org/10.46670/JSST.2023.32.6.340
pISSN 1225-5475/eISSN 2093-7563

Advances in Non-Interference Sensing for Wearable Sensors: Selectively Detecting Multi-Signals from Pressure, Strain, and Temperature

Byung Ku Jung[1], Yoonji Yang[1], and Soong Ju Oh[1,+]

Abstract

Wearable sensors designed for strain, pressure, and temperature measurements are essential for monitoring human movements, health status, physiological data, and responses to external stimuli. Notably, recent research has led to the development of high-performance wearable sensors using innovative materials and device structures that exhibit ultra-high sensitivity compared with their commercial counterparts. However, the quest for accurate sensing has identified a critical challenge. Specifically, the mechanical flexibility of the substrates in wearable sensors can introduce interference signals, particularly when subjected to varying external stimuli and environmental conditions, potentially resulting in signal crosstalk and compromised data fidelity. Consequently, the pursuit of non-interference sensing technology is pivotal for enabling independent measurements of concurrent input signals related to strain, pressure, and temperature, ensuring precise signal acquisition. In this comprehensive review, we present an overview of the recent advances in non-interference sensing strategies. We explore various fabrication methods for sensing strain, pressure, and temperature, emphasizing the use of hybrid composite materials with distinct mechanical properties. This review contributes to the understanding of critical developments in wearable sensor technology that are vital for their ongoing application and evolution in numerous fields.

Keywords: Wearable sensor, Non-interference sensing, Pressure sensor, Temperature sensor, Strain sensor

1. INTRODUCTION

With the rapid development of the Internet of Things (IoT), wearable sensors have received increasing attention in various fields, such as healthcare, soft robotics, and virtual reality motion recognition technology [1-3]. These sensors are incorporated into a range of wearable electronic devices or attached directly to the human epidermis to gather various physical, chemical, and biological signals from individuals and their environment [4-7]. Wearable sensors designed to measure strain, pressure, and temperature play a critical role in monitoring human movement, health status, physiological data, and responses to external stimuli [8-14]. Numerous studies have been conducted to design high-performance wearable sensors using a multitude of materials, including nanoparticles [15-18], carbon nanomaterials [19-21], and organic materials [22-24]. Additionally, innovative device configurations have been developed. Compared with commercial sensors, these sensors exhibit ultra-high sensitivity, enabling them to discern low-intensity biosignals [25-27].

Recently, several studies have focused on performing accurate sensing aimed at reducing the errors and noise signals from sensors. To realize accurate sensing, it is crucial to make conformal contact with the human skin using soft and flexible substrates such as polyimide, polydimethylsiloxane, and Ecoflex [28-32]. However, mechanical flexibility inherent in the substrates of wearable sensors inevitably introduces interference signals in response to various external stimuli and environmental variables, such as pressure, strain, and temperature [33-37]. This interference potential can result in signal crosstalk, thereby compromising the fidelity of data acquisition. Consequently, the development of non-interference sensing technology that enables the independent measurement of responses to concurrent input signals related to strain, pressure, and temperature is of paramount importance for achieving precise signal measurements [38-42].

In this comprehensive review, we present a brief summary of recent developments in non-interference sensing strategies. Specifically, we introduce various non-interference sensing strategies employed in strain, pressure, and temperature sensors that exploit the mechanical properties of hybrid composite materials. Moreover, this review presents an overview of the

[1]Department of Materials Science and Engineering, Korea University 145, Anam-ro Seongbuk-gu Seoul 02841, Republic of Korea
[+]Corresponding author: sjoh1982@korea.ac.kr
(Received: Nov. 3, 2023, Revised: Nov. 23, 2023, Accepted: Nov. 28, 2023)

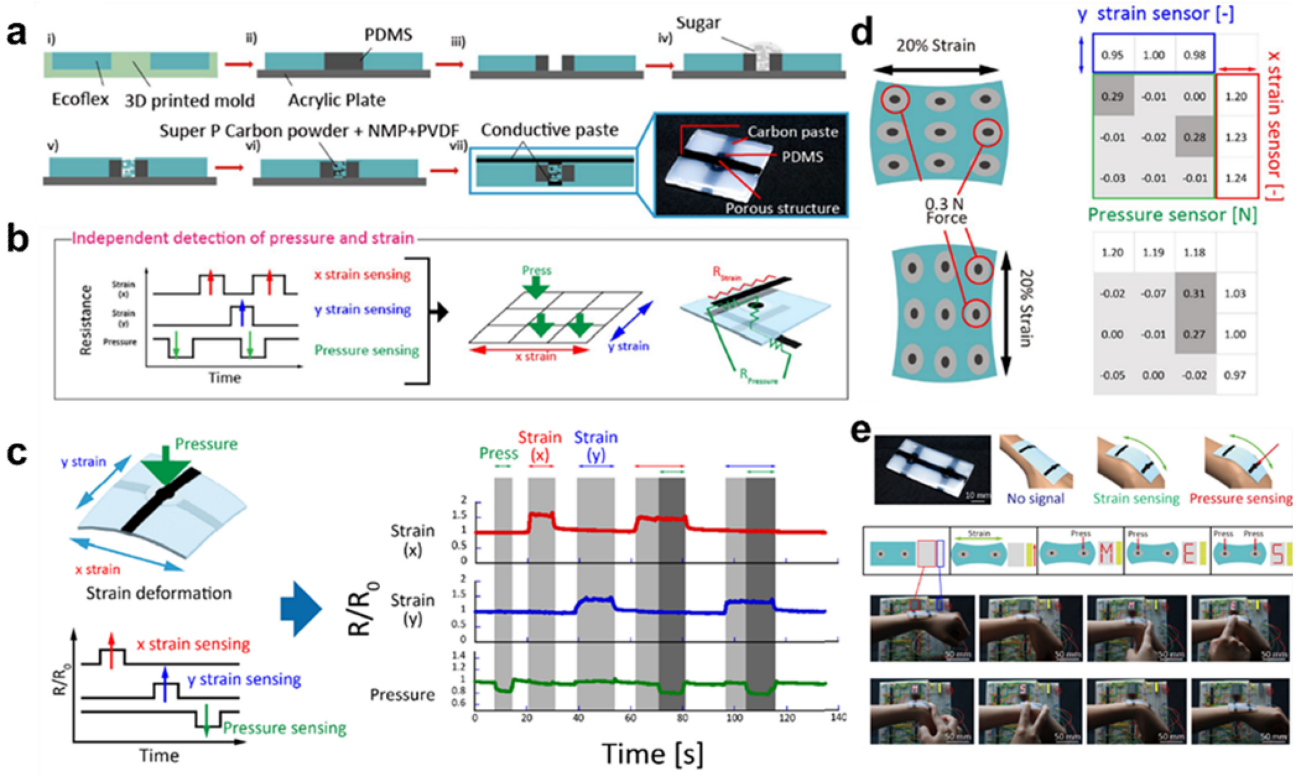

Fig. 1. (a) Fabrication process of a single-pixel device. (b) Schematic of measurement methods and signals of a pressure mapping sensor subjected to strain deformation. (c) Demonstration of independent pressure and x and y strain detection using a single-pixel device. Demonstration of functionality of a multipixel device. (d) Maps of pressure and strain using the 9-pixel device. The device achieved 9-pixel mapping of pressure when subjected to large strains. In addition, it sensed strain using six conductive lines based on a passive matrix. (b) Demonstration of a display controlled by a 2-pixel device with a strain indicator. Reprinted with permission from Ref. [4]. Copyright (2023) Springer Nature.

current challenges and perspectives on future methods for realizing advanced non-interference wearable sensors.

2. RESULTS AND DISCUSSION

2.1 Strain–pressure non-interference sensor

Strain-pressure non-interference sensing requires mechanically separating the strain- and pressure-concentrated regions and inserting suitable sensors at each location. Matsuda et al. developed a strain-pressure non-interference sensor using two different polymer substrates: polydimethylsiloxane (PDMS) and Ecoflex. Fig. 1(a) shows a schematic of the structure and fabrication process of the pressure-sensor noninterference sensor. The areas containing PDMS and Ecoflex were patterned using a 3D mold (Fig. 1(a) (i-iii)). Porous PDMS was created in the central region of the Ecoflex (Fig. 1(a) (iv-vi)), followed by the infusion of a solution containing Super P carbon, fluoropolymer, PVDF, and N-methyl pyrrolidone. The section was used as the pressure sensor. Finally, to detect the X- and Y-strains, column and row electrodes were created on the top and bottom sides of the substrate using carbon paste.

The strain-pressure non-interference sensor was designed with a central pressure-detecting region composed of relatively rigid PDMS and surrounded by soft Ecoflex. The design enables efficient minimization of strain in the pressure sensor area by concentrating it on a softer Ecoflex section, where the carbon paste electrodes are placed in columns and rows. The upper and lower parts of the Ecoflex were coated with carbon paste along the x- and y-axes to facilitate the measurement of changes in resistance in response to strain. Conversely, when pressure is applied, it becomes concentrated in the hard PDMS region, transmitting pressure to the pressure sensor within the PDMS. The utilization of hard silicon PDMS and a soft silicon Ecoflex composite substrate enabled the sensor to decouple the regions in which the mechanical strain and pressure are concentrated. Fig. 1(b) shows that the sensor independently measures the applied

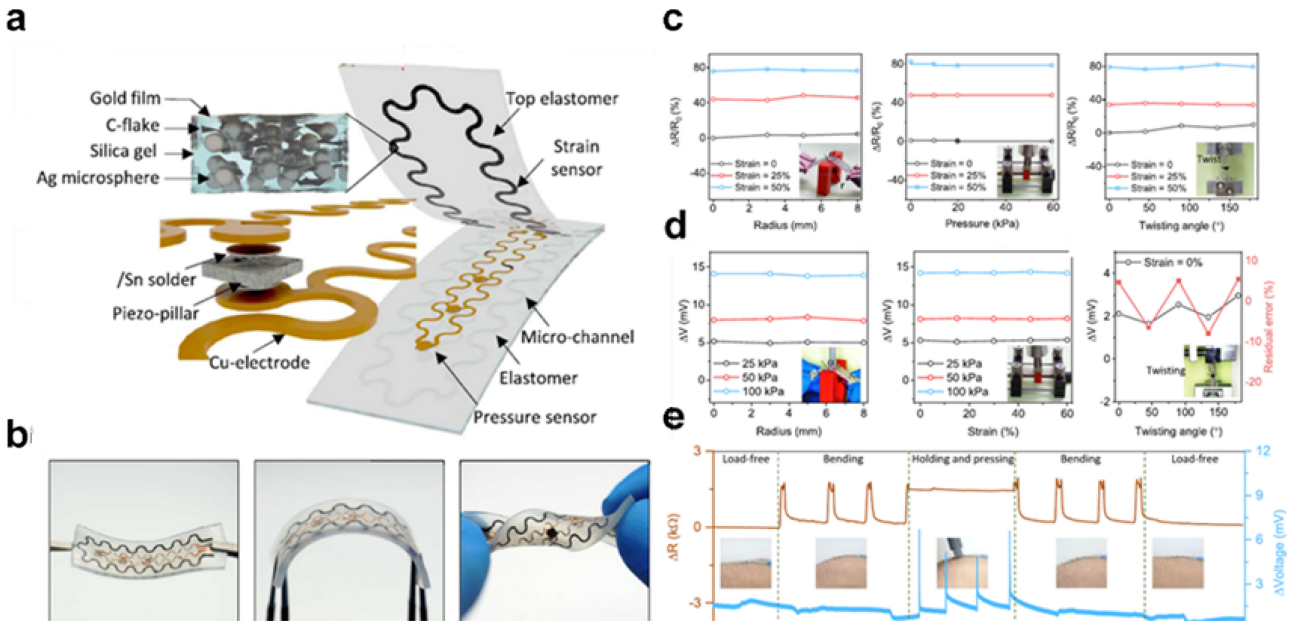

Fig. 2. (a) Design concept of the integrated strain-pressure integrated sensor patch (ISP). (b) Images of the ISP in elastic compliance under no load (left), bending (middle), and torsion (right). Scale bar: 5 mm. (c) Torsional, pressure, and bending insensitivity tests of the strain sensor at different torsional, compressive stress, and conformal radius states for a certain tensile strain, respectively. (d) Off-axis deformation tests at different twist angle states, tensile strain, and conformal radius. (e) Strain and pressure response of the ISP under continuous deformation. Reprinted with permission from Ref. [44]. Copyright (2023) Springer Nature.

pressures and strains. The strain and pressure were measured by monitoring the resistance changes in the PDMS composite and carbon electrodes. The resistance changes of the pressure sensor can be measured using vertically connected X- and Y-axis carbon electrodes and strain sensors arranged along the X- and Y- axes to measure the strain changes in their respective directions and pressure sensors. Owing to the larger resistance of the pressure sensor compared with that of the carbon electrodes, the strain-induced resistance changes in the carbon electrodes did not significantly affect the resistance changes in the pressure sensor.

Strain and pressure were simultaneously applied to the strain-pressure non-interference sensor, and the corresponding signals are illustrated in Fig. 1(c). When subjected to strain, a significant increase was observed in the resistances of the X- and Y-axis strain sensors, whereas the pressure sensor did not exhibit any change in resistance. Conversely, when subjected to pressure, the porous structure of the pressure sensor was compressed, which resulted in a decrease in resistance, whereas the strain sensor did not exhibit a change in resistance under the same conditions. These results underscore the independent performance of the strain and pressure sensors. Fig. 1(d) presents the quantitative resistance changes in a 3 × 3 array of the strain-pressure non-interference sensor when exposed to simultaneous pressure and strain. An increase in resistance along the X- and Y-axes was observed when the device experienced strains in the X- and Y-directions, respectively. Conversely, the resistance of the pressure sensors decreased when the device was subjected to pressure. This demonstrated the independent sensing of pressure and strain stimuli when applied concurrently. Finally, the performance of the strain-pressure non-interference sensor array was demonstrated by affixing it to the wrist, as shown in Fig. 1(e). The results revealed that the sensor was capable of accurately distinguishing between pressure and strain stimuli in real time. The light-emitting diode (LED) and display components were controlled separately in response to the pressure and strain signals.

Xu et al. developed a strain-pressure non-interference sensor, referred to as intrinsic strain pressure (ISP), using two different types of materials: physically rigid ceramic and soft serpentine-patterned nanocomposite. These materials were used to fabricate the pressure and strain sensor areas of ISP. Similar to the sensor developed by Matsuda et al. (Fig. 1), the applied pressure was concentrated on the rigid ceramic material, while the applied strain was concentrated on the soft nanocomposite. In addition, the serpentine pattern of the soft nanocomposite protected the ISP sensor from bending and twisting. A schematic of the ISP sensor is shown in Fig. 2(a), which illustrates the presence of two distinct layers: a top strain sensor layer and a bottom pressure sensor layer. Fig. 2(b) presents images that demonstrate the bending and

twisting of the ISP sensor.

The strain sensor comprised carbon nanoparticles, an Au film, and an Ag microsphere nanocomposite, which exhibited a low initial resistance and high sensitivity. The nanocomposite was patterned into a serpentine geometry via laser-assisted patterning. The objective of this design is to minimize resistance changes by reducing the stress during bending and twisting. Fig. 2(c) shows the resistance changes in the strain sensor under various bending, pressure, and twisting conditions. No significant resistance changes were observed under any of the tested conditions. Conversely, the strain sensor exhibits substantial resistance changes under strain conditions of 0%, 25%, and 40%. The gauge factors of the strain sensors ranged from approximately 1.23 1.75. Rigid ceramic material PZT-5 was used as the piezoelectric-type pressure sensor. Fig. 2(d) shows the resistance changes in the pressure sensor under various bending, twisting, and strain conditions. No resistance changes were observed under the bending, straining, or twisting conditions. In contrast, significant changes in the resistance were observed in response to applied pressures of 25, 50, and 100 kPa. Moreover, the pressure sensor exhibited high linearity ($R^2 > 0.99$) with a wide sensing range up to approximately 100 kPa and a sensitivity (S) of 2.88 kPa^{-1}. The sensitivity (S) was calculated by dividing the normalized voltage change by the pressure change.

Fig. 2(e) illustrates the ability of the ISP sensor, to perform non-interference sensing by effectively distinguishing between the applied strain and pressure when attached to the wrist. The ISP sensor was subjected to strain under the "Bending" condition and concurrently to both strain and pressure stimuli under the "Holding and pressurizing" condition. During the “Bending” process, no voltage changes were observed in the pressure sensor, whereas the applied strain successfully changed the resistance of the strain sensor. In the “Holding and pressurizing” process, the strain sensor maintains a constant resistance while effectively detecting a strong pressure signal. Once the pressure was relieved, the sensor continued to detect the strain signal, thereby confirming its ability to detect both tension and pressure without any mutual interference.

2.2 Pressure–temperature non-interference sensor

In the pursuit of temperature-pressure non-interference sensing, several studies have employed multiple types of sensors, mostly combining capacitive- and resistive-type sensors. Li et al. introduced a novel solution for developing temperature-pressure non-interference sensors, referred to as metal-organic frameworks or microstructured mixed cellulose (MOF-MSMC). These sensors comprise a capacitive-type temperature sensor based on MOFs and a resistive-type pressure sensor based on MSMC. The capacitive sensor effectively detects the temperature gradients by generating a potential ($V_{thermal}$), and the resistive sensor measured the resistance changes in response to the applied pressure.

Fig. 3(a) illustrates the mechanism of temperature and pressure sensing in the MOF–MSMC. A capacitive-type MOF temperature sensor generates a voltage in response to temperature changes by leveraging the thermoelectric effect, and the voltage is measured for temperature sensing purposes. The MSMC is employed as a high-performance piezoresistive pressure sensor. When pressure is applied to the MSMC, its microstructure undergoes significant changes, resulting in substantial changes in resistance. However, the application of pressure to the microporous structure did not generate a significant voltage, $V_{thermal}$. Additionally, the sensors in the MOF-MSMCs subjected to temperature variations exhibited substantial changes in $V_{thermal}$, whereas the pressure sensor did not exhibit significant variations in resistance.

Fig. 3(b) presents a quantitative assessment of the temperature sensor performance. The figure shows the measured $V_{thermal}$ generated within the MOF-MSMC in response to a temperature gradient of 0–40 K. As the temperature gradient increases, the thermal voltage exhibits a linear increase. Sensitivity, as determined from the slope of the graph, is 57.1 μVK^{-1}. Fig. 3(c) presents a quantitative evaluation of the performance of the pressure sensor. It illustrates the relative current variation of the MOF-MSMC sensor when subjected to different pressure stimuli, demonstrating the capability of the sensor to detect pressures of up to 300 kPa. The MOF–MSMC sensor exhibits notable sensitivity, with values reaching 61.61 kPa^{-1} within a pressure range of 32.02 kPa, 10.94 kPa^{-1} between 32.02–70.12 kPa, 4.02 kPa^{-1} between 70.12-133.33 kPa, 1.08 kPa^{-1} between 133.33–202.10 kPa, and 0.36 kPa^{-1} within 202.10−300 kPa. Moreover, as shown in Fig. 3(c) and 3d, the non-interference performance of the MOS-MSMC was investigated under various pressure and temperature conditions. The pressure-current graphs exhibited nearly identical behavior under different temperature gradients of 0, 15, and 30 K, and it was confirmed that $V_{thermal}$ also yielded consistent output values when the pressure conditions varied within 20 kPa. These results indicate that temperature variations and pressure conditions do not exert a mutual influence.

Fig. 3(e) and 3(f) depict the conceptualization of the 3 × 3 MOS-MSMC array used to simulate real-world scenarios of non-interference sensing (dual-sensing mode). In Fig. 3(e), two water bottles with different temperatures but identical weights were

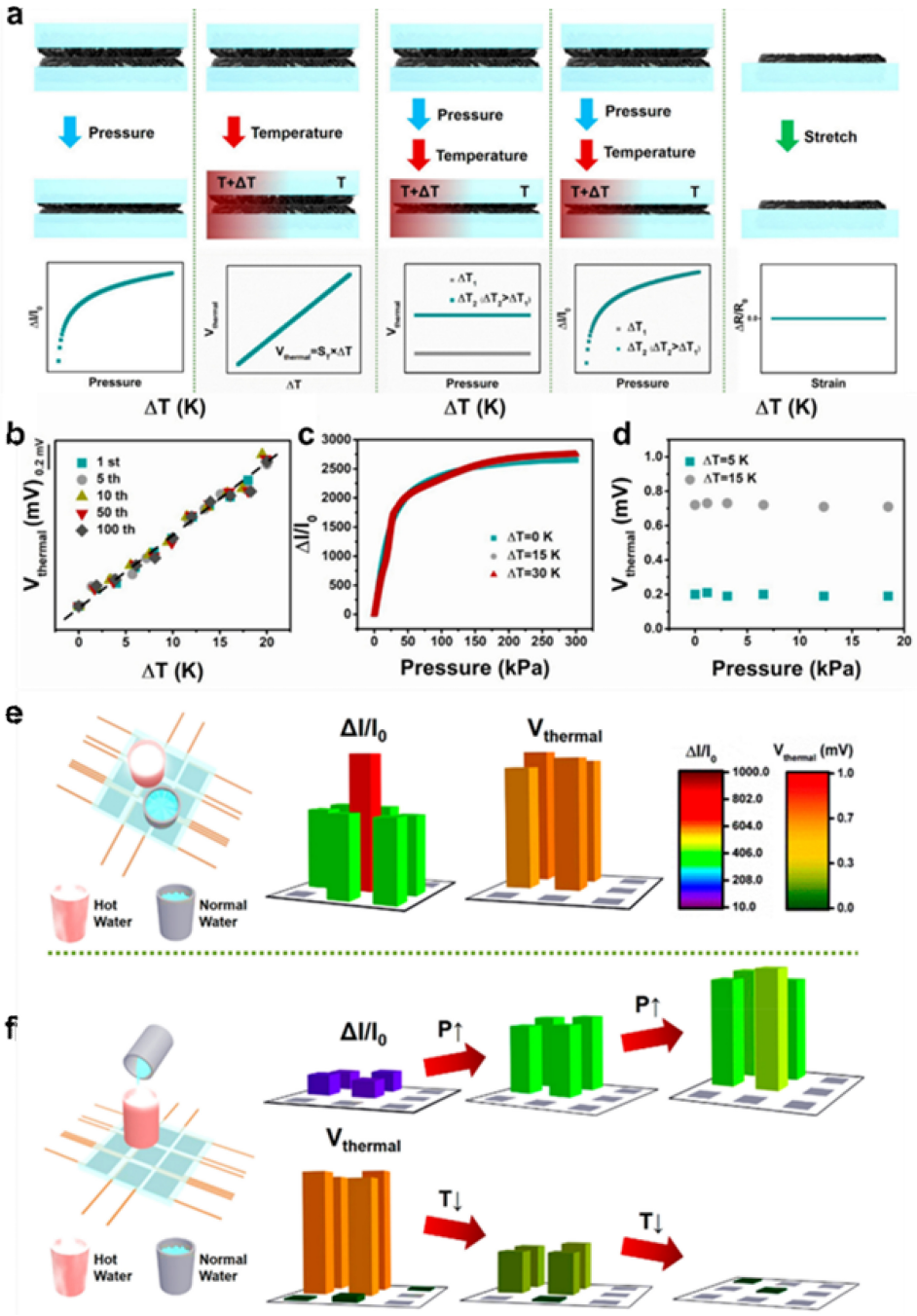

Fig. 3. (a) Schematics of the response mechanism of the metal-organic framework (MOF)-microstructure mixed cellulose (MSMC) sensor. (b) Output thermal voltage variation of the MOF–MSMC-5h sensor under the 1st, 5th, 10th, 50th, and 100th heating cycles with a temperature gradient of 20 K. (c) Relative current variation versus pressure curves of the MOF-–MSMC-5h sensor under different temperature gradients of 0, 15, and 30 K. (d) Output thermal voltage variation versus pressure-dotted curves under constant temperature gradients of 5 K (bottom) and 15 K (top). (e, f) Dual-modal applications of the MOF–MSMC-5h sensor-based sensing array. Reprinted with permission from Ref. [46]. Copyright 2021 American Chemical Society.

placed at different positions, and the resulting resistance changes and $V_{thermal}$ measurements were recorded using the pressure sensor array. The resistance changes corresponded precisely to the positions of the two bottles, whereas $V_{thermal}$ was only detected at the site where hot water was present. Fig. 3(f) presents real-time measurements of the resistance changes and $V_{thermal}$ while adjusting the amount of cold water in a bottle containing hot water. In this case, the resistance increases with the weight of the bottle, and $V_{thermal}$ decreases as the temperature of the bottle decreases. These demonstrations conclusively establish the non-

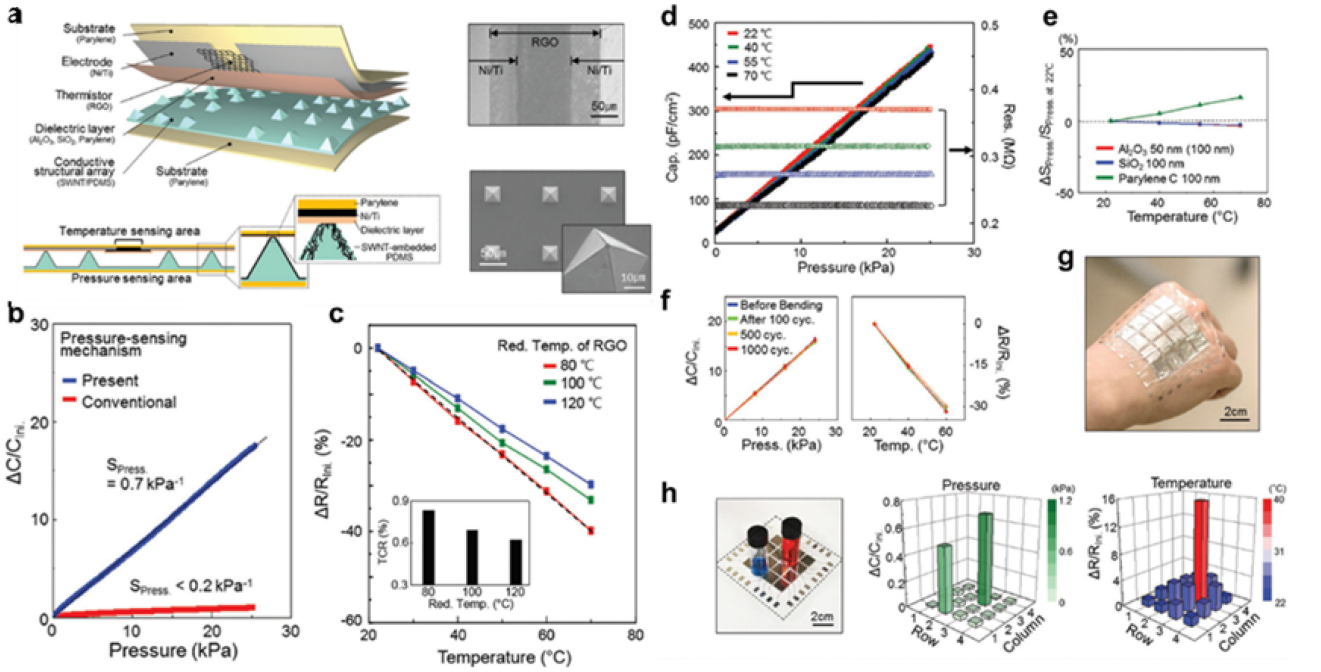

Fig. 4. (a) Schematic illustration of stimulus-discriminating and linearly sensitive bimodal E-skin. (b) Pressure-response plots of the E-skin compared with the device that has a conventional capacitive mechanism. (c) Temperature-response plots illustrating the effect of reduction. (c) Temperature-response plots. (d, e) Simultaneous sensing performance of the E-skin with stimulus discriminability and high/linear sensitivity under mixed stimulation. (f) Pressure and temperature-response curves after a cyclic bending test with the curvature of 3R. (g) Photograph of the large-scaled E-skin with 4 × 4 pixels on the back of a hand. (h) Photograph captured when measuring the pressure/temperature-sensing capability and the results on pressure/temperature of two vials with different weights and temperatures. Reprinted with permission from Ref. [47]. Copyright 2018 WILEY-VCH Verlag GmbH & Co. KGaA, Weinheim.

interference performance of the MOS–MSMC with respect to pressure and temperature.

Geun et al. realized temperature-pressure non-interference sensors using a capacitive-type pressure sensor and a resistive-type temperature sensor. Fig. 4(a) depicts the structure of the temperature-pressure non-interference sensor. The sensor comprises an upper resistive-type temperature sensor that uses reduced graphene oxide (RGO) and a lower capacitive-type pressure sensor that uses a single-walled carbon nanotube/polydimethylsiloxane (SWNT/PDMS) composite as the spacer. The sensors are separated using a dielectric layer.

A truncated pyramidal microstructure with a top area of 2.1 μm × 2.1 μm and a bottom area of 30 μm × 30 μm was designed to realize the pressure sensor. Subsequently, SWNTs were coated onto the top surface of the microstructure to serve as an electrode. Based on the magnitude of the pressure, the area of contact between the pyramidal structure and the dielectric changes, resulting in variations in the capacitance measured between the SWNT and Ti/Ni electrodes. Fig. 4(b) presents the measured changes in capacitance for the pressure sensor, revealing a high sensitivity of 0.7 kPa^{-1}. Notably, this approach exhibits a significantly higher sensitivity than the conventional method of measuring capacitance based on changes in the electrode separation distance (conventional capacitance-type sensor: 0.2 kPa^{-1}). To realize a resistive-type temperature sensor, RGO was deposited between the Ni/Ti electrodes at a spacing of 100 μm. Fig. 4(c) shows the temperature coefficient resistance (TCR) of RGO as a function of the reduction temperature. During RGO fabrication, the reduction of hydrazine hydrate vapor was performed at various temperatures. As the reduction process temperature increased, a more favorable reduction reaction was facilitated, and the restoration of the sp2 domain of graphene was enhanced, thereby lowering the activation energy for charge transfer. Consequently, the absolute value of TCR maximized at a lower temperature of 80 °C.

Fig. 4(d) shows the simultaneous application of external stimuli of temperature and pressure to the sensor to demonstrate the decoupling between the upper temperature sensor and the lower pressure sensor. Notably, the pressure-capacitance curve of the pressure sensor exhibited minimal changes in response to temperature variations. Conversely, the resistance of RGO measured by the temperature sensor remained constant despite the

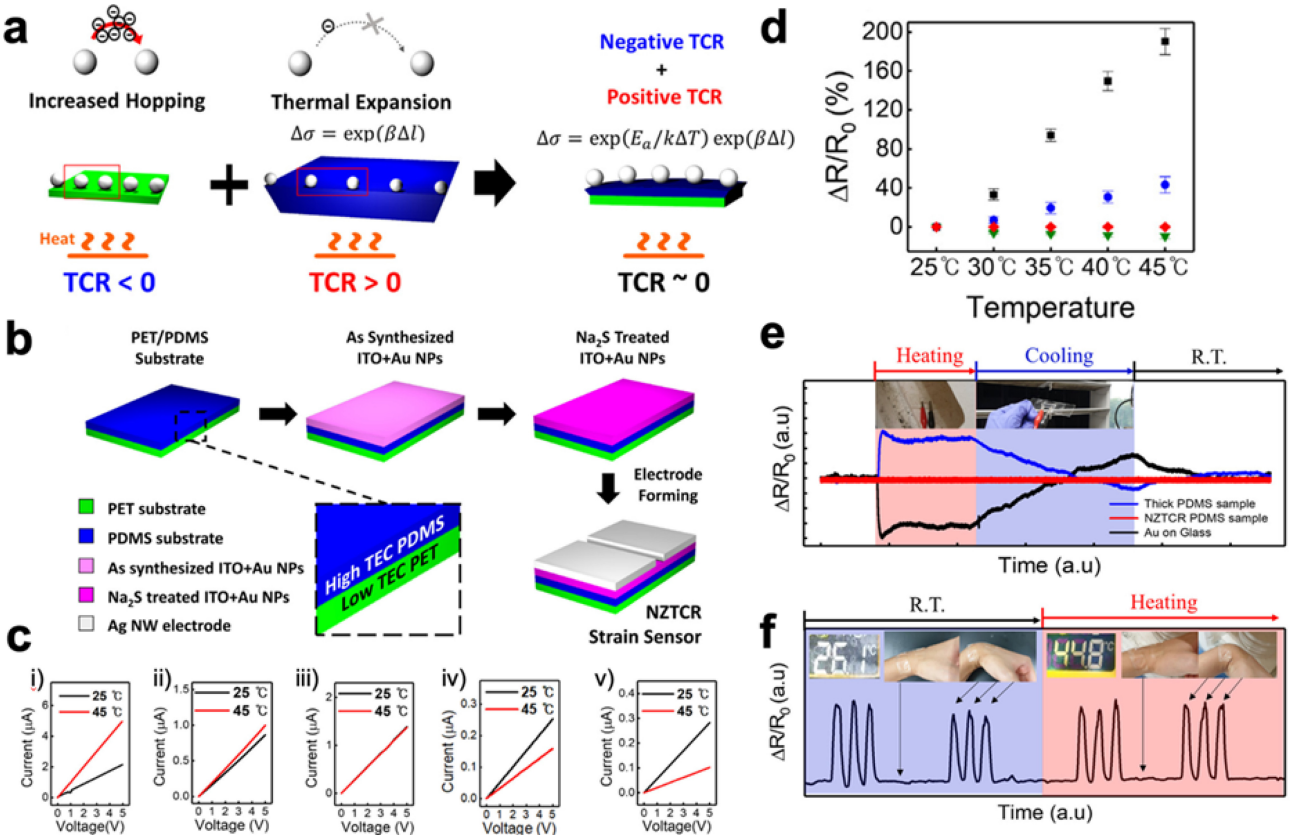

Fig. 5. (a) Design concept of the near-zero temperature coefficient of resistance (NZTCR). (b) Fabrication process of the NZTCR transparent strain sensor device. (c) Current-voltage (I–V) characteristics of polyethylene terephthalate (PET) only and PDMS of 0.35 mm, 0.8 mm, 1.2 mm, and 4.0 mm samples. (d) Changes in the ratio of resistance of PDMS 4.0 (black), 1.2 (blue), 0.8 (red), and 0.35 (green) samples measured at 5 °C intervals from 25 to 45 °C. (e) Schematic image of the changing interparticle distance owing to the thermal expansion of the PET (black), moderate (blue), and thick (red) PDMS substrates at 25 °C and 45 °C, respectively. (f) Real-time bending test with an NZTCR strain sensor under room temperature (blue) and a hot environment (red). Reprinted with permission from Ref. [48]. Copyright 2021, American Chemical Society.

change in the applied pressure magnitude. These results confirm that a non-interference sensor was successfully fabricated, in which the pressure and temperature were completely decoupled. Fig. 4(e) illustrates the variation in the dielectric constant of the dielectric material with the temperature. Al_2O_3 and SiO_2 consistently maintained stable dielectric constants across all temperature ranges. Fig. 4(f) depicts the changes in capacitance owing to pressure and variations in the resistance owing to temperature after the sensors were subjected to 0, 100, 500, and 1000 cycles of pressure and temperature fluctuations. Remarkably, even after 1000 cycles, the sensors exhibited consistent performance.

Fig. 4(g) shows a photograph of the 4 × 4 sensor array, where two vials—one red (10 g) with a temperature of 40 °C and the other blue (7 g) with a temperature of 22 °C, were placed on the E-skin array in practical application. This enabled the simultaneous measurement and discrimination of pressure and temperature when two vials with different weights and temperatures were positioned on the E-skin array.

2.3 Strain–temperature non-interference sensor

To realize strain-temperature non-interference sensing, new sensing materials have been designed using hybrid materials to obtain a near-zero temperature coefficient of resistance (NZTCR) and high sensitivity to strain stimuli. Park et al. designed NZTCR materials by controlling the hopping transport of nanoparticles and the thermal expansion characteristics of a polymer substrate to develop a temperature-strain non-interference sensor at the material/structural levels. Fig. 5(a) illustrates the operating principle of the temperature-strain non-interference sensor. The nanoparticle thin film inherently possesses a negative TCR, causing the resistance to decrease as the temperature increases owing to the enhanced hopping probability. Conversely, because

the polymer substrate thermally expanded as the temperature increased, the distance between the nanoparticles also increased, resulting in an increase in their resistance. To manufacture a substrate for the implementation of the NZTCR using the two aforementioned principles, a dual-layer polymer substrate was fabricated using polyethylene terephthalate (PET) as the anchoring layer to limit the thermal expansion of PDMS. NZTCR was successfully achieved by adjusting the thermal expansion coefficient (TEC) and optimizing the substrate thickness. Fig. 5(b) illustrates the fabrication process of the NZTCR transparent strain sensor. The process involved the following steps: production of an optimized dual-layer polymer substrate, spin coating of the substrate with an ITO/Au nanoparticle mixture, ligand exchange of the nanoparticles with an Na_2S solution to create a transparent and highly conductive sensing layer and spray coating with Ag nanowires serving as electrodes.

Current-voltage (I–V) curves varying with PDMS thickness at 25 °C and 45 °C were analyzed to investigate the electrical and thermo-mechanical characteristics, as shown in Fig. 5(c). (i) For the PET-only sample, as the temperature increased from 25 °C to 45 °C, the resistance decreased by 56.4%. Furthermore, the TCR tendencies were examined with respect to the adjustment of PDMS thickness. (ii) For PDMS 0.35, the resistance decreased by 13.9% as the temperature increased. (iii) PDMS 0.8 exhibited a minimal response to temperature changes, with the resistance fluctuating by only 0.0016%. (iv-v) In contrast, for PDMS 1.2 and 4.0, the resistance increased with the temperature, and the percentage changes were 59.2% and 178%, respectively. Sensitivity to temperature can be expressed through TCR, calculated using the formula TCR = $(\Delta R/R_0)/\Delta T$. Fig. 5(d) illustrates the percentage of resistance changes with temperature variations from 25 °C to 45 °C. The TCR values for the PET-only sample and PDMS 0.35 were calculated as -2.82×10^{-2} and -6.97×10^{-3} K^{-1}, respectively, representing a negative TCR. PDMS 0.8 had a value close to zero at -7.989×10^{-7} K^{-1}, while PDMS 1.2 and 4.0 exhibited positive TCR values of 2.96×10^{-2} and 8.88×10^{-2} K^{-1}, respectively.

In Fig. 5(e), the resistance change rates of the Au-on-glass (negative TCR), NZTCR PDMS, and thick PDMS (positive TCR) samples are presented in real time under hot (red area) and cold (blue area) ambient conditions. When exposed to hot ambient conditions, the Au-on-glass samples demonstrated a substantial decrease in resistance, whereas the thick PDMS samples exhibited a significant increase. In contrast, the optimized NZTCR PDMS sample maintained stable resistance under hot ambient conditions. When exposed to cold ambient conditions, resistance changes were observed in the opposite direction; however, the NZTCR PDMS sample continued to exhibit a stable resistance. Finally, Fig. 5(f) shows the tests and corresponding results conducted to verify the ability of the sensor to detect strain while remaining insensitive to temperature changes. The optimized sensor was subjected to repeated bending and stretching using wrist movements. Regardless of the environmental temperature, the resistance changed only when the wrist was bent and returned to its original state when straightened, confirming its reliable performance as a temperature–strain non-interference sensor.

Choi et al. developed NZTCR materials by doping poly(3,4-ethylenedioxythiophene):poly(styrene sulfonic acid) (PEDOT:PSS) thin films with dimethyl sulfoxide (DMSO) to modulate variable range hopping (VRH) transport resulting from disordered polymer structures. Fig. 6(a) illustrates the mechanism of creating the sensing layer via the secondary doping of DMSO into PEDOT:PSS thin films. The conductive polymer, PEDOT:PSS, exhibited improved conductivity and reduced resistance with increasing temperature, indicating a negative TCR. The polymer was doped with DMSO as a polar solvent because of its positive TCR, resembling metal-like behavior when subjected to polar solvents or acid treatment. The critical point of charge transport was determined by adjusting the secondary doping concentration of DMSO, and the electrical properties and TCR dependence of PEDOT:PSS were investigated.

Fig. 6(b) presents the temperature-dependent conductivity changes in the PEDOT:PSS thin films doped with different concentrations of DMSO. I–V curves were measured for pristine and doped PEDOT:PSS thin films at 273 K, 298 K, and 323 K, respectively. Pristine samples exhibited a significant increase in current as the temperature increased from 273 K to 323 K. When doped with 1 and 2 vol %, DMSO increased the current, albeit by a small amount. However, in the case of 3% DMSO doping, there was little change in the current despite the temperature variations. Furthermore, as the DMSO concentration increased to 4% and 5%, the current decreased with increasing temperature. In the insets of Fig. 6(b), each case is magnified to show the current changes more accurately.

As described in Fig. 5, TCR can be defined as TCR = $(\Delta R/R_0)/\Delta T$. Fig. 6(c) displays the TCR variation with respect to the DMSO concentration. The TCR values for pristine and 1–5% DMSO-doped samples were -7.2×10^{-3}, -3.0×10^{-3}, -8.4×10^{-4}, 9.3×10^{-5}, 5.7×10^{-4}, and 9.4×10^{-4} K^{-1}, respectively. The significant temperature dependence of the resistance of the pristine PEDOT:PSS samples can be attributed to the thermally activated VRH transport. This trend decreases as the DMSO

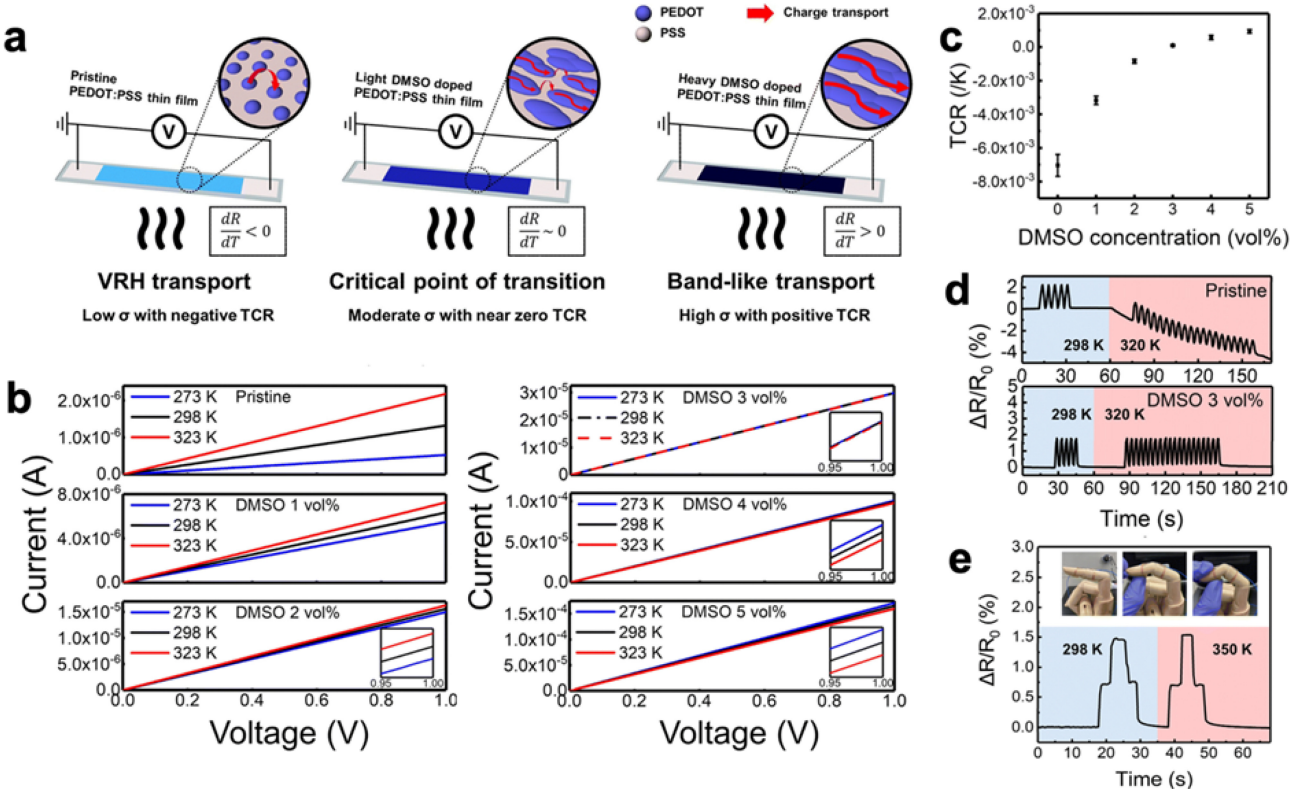

Fig. 6. (a) Schematic of the morphological change owing to the transition of transport behavior in poly(3,4-ethylenedioxythiophene):poly(styrene sulfonic acid) dimethyl sulfoxide (PEDOT:PSS DMSO) induced by secondary doping. (b) Pristine and doped with 1–5 vol% DMSO. (c) TCR of PEDOT:PSS thin films versus DMSO doping concentrations. (d) Collected strain signal of the pristine and 3 vol% DMSO-doped PEDOT:PSS thin-film strain sensor at ambient temperature. (e) Finger bending test of the 3 vol% DMSO-doped PEDOT:PSS thin-film strain sensor at ambient temperature. Reprinted with permission from Ref. [44]. Copyright 2023, Royal Society of Chemistry.

concentration increases, and the behavior shifts from negative to positive TCR values with only 3% DMSO doping. In Fig. 6(d), the resistance variations of a pristine thin film with negative TCR behavior and a 3 vol% DMSO-doped PEDOT:PSS thin film strain sensor with near-zero TCR behavior are shown under the application of repetitive strain at 298 K and 320 K, respectively. When the pristine samples were subjected to bending strain, the electronic response was highly sensitive to temperature, and the resistance decreased drastically as the temperature increased from 298 K to 320 K. In contrast, for the 3%-DMSO-doped samples, the change in resistance owing to strain was constant, even in high-temperature environments. In other words, sensors doped with the optimized concentration could only detect strain-related signals without interference from temperature changes. To use this sensor in practical applications, we attached a 3%-DMSO-doped PEDOT:PSS thin-film strain sensor to a prosthetic hand and conducted finger-bending tests, as shown in Fig. 6(e). The change in resistance was proportional to the degree of bending when the fingers were bent in two steps at 298 K. Additionally, even when subjected to a temperature of 350 K, the changes in resistance remained consistent, demonstrating the ability of the sensor to accurately detect strains without temperature interference.

Considering that wearable sensors are exposed to a range of external stimuli beyond pressure, temperature, and strain, it is imperative to advance research towards achieving non-interference, particularly in distinguishing diverse stimuli like chemical inputs. Future studies should focus on enhancing the sensors' ability to seamlessly differentiate and operate amidst a broader spectrum of stimuli.

3. CONCLUSIONS

Wearable sensors have been fabricated on soft substrates to ensure conformal contact with the human skin, which frequently results in signal distortion caused by other external stimuli. Therefore, the development of accurate and reliable non-interference sensing technology has emerged as a significant

challenge in the field of wearable sensors. In this comprehensive review, we presented the latest advancements in non-interference sensing technology, focusing on three critical factors: strain, pressure, and temperature. Our review elucidated various non-interference strategies aimed at discriminating between two different signals, including strain-pressure, pressure-temperature, and strain-temperature interactions. Although substantial progress has been made in these areas, there remains a pressing need for further developing non-interference technologies capable of simultaneously decoupling three or more physical stimuli. We believe that this review provides valuable guidelines for the implementation of non-interference sensing in multifunctional wearable sensors.

ACKNOWLEDGMENT

B. K. J. and Y. Y. contributed equally to this work. This research was supported by (2022R1A2C4001517) Basic Science Research Program through the National Research Foundation of Korea (NRF), funded by the Ministry of Science, ICT, and Future Planning.

REFERENCES

[1] T. Xu, W. Wang, X. Bian, X. Wang, X. Wang, J. K. Luo, and S. Dong, "High resolution skin-like sensor capable of sensing and visualizing various sensations and three dimensional shape", *Sci. Rep.*, Vol. 5, No. 1, pp. 1-9, 2015.

[2] A. B. Vallbo, K. E. Hagbarth, H. E. Torebjork, and B. G. Wallin, "Somatosensory, proprioceptive, and sympathetic activity in human peripheral nerves", *Physiol. Rev.*, Vol. 59, No. 4, pp. 919-957, 1979.

[3] R. C. Webb, A. P. Bonifas, A. Behnaz, Y. Zhang, K. J. Yu, H. Cheng, M. Shi, Z. Bian, Z. Liu, Y. S. Kim, W.-H. Yeo, J. S. Park, J. Song, Y. Li, Y. Huang, A. M. Gorbach, and J. A. Rogers, "Ultrathin conformal devices for precise and continuous thermal characterization of human skin", *Nat. Mater.*, Vol. 12, No. 10, pp. 938-944, 2013.

[4] J. Tegin and J. Wikander, "Tactile sensing in intelligent robotic manipulation - A review", *Ind. Rob.*, Vol. 32, No. 1, pp. 64-70, 2005.

[5] R. S. Dahiya, P. Mittendorfer, M. Valle, G. Cheng, and V. J. Lumelsky, "Directions toward effective utilization of tactile skin: A review", *IEEE Sens. J.*, Vol. 13, No. 11, pp. 4121-4138, 2013.

[6] M. L. Hammock, A. Chortos, B. C. K. Tee, J. B. H. Tok, and Z. Bao, "25th anniversary article: The evolution of electronic skin (E-Skin): A brief history, design considerations, and recent progress", *Adv. Mater.*, Vol. 25, No. 42, pp. 5997-6038, 2013.

[7] Y. Lee, J. Park, A. Choe, S. Cho, J. Kim, and H. Ko, "Mimicking Human and Biological Skins for Multifunctional Skin Electronics", *Adv. Funct. Mater.*, Vol. 30, No. 20, pp. 1904523(1)-1904523(32), 2020.

[8] J. Ma, P. Wang, H. Chen, S. Bao, W. Chen, and H. Lu, "Highly Sensitive and Large-Range Strain Sensor with a Self-Compensated Two-Order Structure for Human Motion Detection", *ACS Appl. Mater. Interfaces*, Vol. 11, No. 8, pp. 8527-8536, 2019.

[9] A. Koivikko, V. Lampinen, M. Pihlajamäki, K. Yiannacou, V. Sharma, and V. Sariola, "Integrated stretchable pneumatic strain gauges for electronics-free soft robots", *Commun. Eng.*, Vol. 1, No. 1, pp. 14(1)-14(10), 2022.

[10] K. Xu, Y. Lu, S. Honda, T. Arie, S. Akita, and K. Takei, "Highly stable kirigami-structured stretchable strain sensors for perdurable wearable electronics", *J. Mater. Chem. C*, Vol. 7, No. 31, pp. 9609-9617, 2019.

[11] R. Nur, N. Matsuhisa, Z. Jiang, M. O. G. Nayeem, T. Yokota, and T. Someya, "A Highly Sensitive Capacitive-type Strain Sensor Using Wrinkled Ultrathin Gold Films", *Nano Lett.*, Vol. 18, No. 9, pp. 5610-5617, 2018.

[12] Q. Yu, R. Ge, J. Wen, T. Du, J. Zhai, S. Liu, L. Wang, and Y. Qin, "Highly sensitive strain sensors based on piezotronic tunneling junction", *Nat. Commun.*, Vol. 13, No. 1, pp. 778(1)-778(9), 2022.

[13] J. Bang, W. S. Lee, B. Park, H. Joh, H.K. Woo, S. Jeon, J. Ahn, C. Jeong, T. il Kim, and S. J. Oh, "Highly Sensitive Temperature Sensor: Ligand-Treated Ag Nanocrystal Thin Films on PDMS with Thermal Expansion Strategy", *Adv. Funct. Mater.*, Vol. 29, No. 32, pp. 1-8, 2019.

[14] S. C. B. Mannsfeld, B. C-K. Tee, R. M. Stoltenberg, C. V. H-H. Chen, S. Barman, B. V. O. Muir, A. N. Sokolov, C. Reese, and Z. Bao, "Highly sensitive flexible pressure sensors with microstructured rubber dielectric layers", *Nat. Mater.*, Vol. 9, No. 10, pp. 859-864, 2010.

[15] J. Ahn, S. Jeon, W. S. Lee, H. K. Woo, D. Kim, J. Bang, and S. J. Oh, "Chemical Effect of Halide Ligands on the Electromechanical Properties of Ag Nanocrystal Thin Films for Wearable Sensors", *J. Phys. Chem. C*, Vol. 123, No. 29, pp. 18087-18094, 2019.

[16] J. Ahn, S. Jeon, H. K. Woo, J. Bang, Y. M. Lee, S. J. Neuhaus, W. S. Lee, T. Park, S. Y. Lee, B. K. Jung, H. Joh, M. Seong, J. H. Choi, H. G. Yoon, C. R. Kagan, and S. J. Oh, "Ink-Lithography for Property Engineering and Patterning of Nanocrystal Thin Films", *ACS Nano*, Vol. 15, No. 10, pp. 15667-15675, 2021.

[17] H. Joh, W. S. Lee, M. S. Kang, M. Seong, H. Kim, J. Bang, S. W. Lee, M. A. Hossain, and S. J. Oh, "Surface Design of Nanocrystals for High-Performance Multifunctional Sensors in Wearable and Attachable Electronics", *Chem. Mater.*, Vol. 31, No. 2, pp. 436-444, 2019.

[18] H. Kim, S. W. Lee, H. Joh, M. Seong, W. S. Lee, M. S. Kang, J. B. Pyo, and S. J. Oh, "Chemically Designed Metallic/Insulating Hybrid Nanostructures with Silver Nanocrystals for Highly Sensitive Wearable Pressure Sensors", *ACS Appl. Mater. Interfaces,* Vol. 10, No. 1, pp. 1389-1398, 2018.

[19] A. Kaidarova, M. A. Khan, M. Marengo, L. Swanepoel, A.

Przybysz, C. Muller, A. Fahlman, U. Buttner, N. R. Geraldi, R. P. Wilson, C. M. Duarte, and J. Kosel, "Wearable multifunctional printed graphene sensors", *Npj Flex. Electron.*, Vol. 3, No. 1, pp. 15(1)-15(10), 2019.

[20] Y. Qiao, X. Li, T. Hirtz, G. Deng, Y. Wei, M. Li, S. Ji, Q. Wu, J. Jian, F. Wu, Y. Shen, H. Tian, Y. Yang, and T. L. Ren, "Graphene-based wearable sensors", *Nanoscale*, Vol. 11, No. 41, pp. 18923-18945, 2019.

[21] Q. Zheng, J. hun Lee, X. Shen, X. Chen, and J. K. Kim, "Graphene-based wearable piezoresistive physical sensors", *Mater. Today*, Vol. 36, pp. 158-179, 2020.

[22] H. J. Kim, A. Thukral, and C. Yu, "Highly sensitive and very stretchable strain sensor based on a rubbery semiconductor", *ACS Appl. Mater. Interfaces*, Vol. 10, No. 5, pp. 5000-5006, 2018.

[23] Y. F. Wang, T. Sekine, Y. Takeda, J. Hong, A. Yoshida, H. Matsui, D. Kumaki, T. Nishikawa, T. Shiba, T. Sunaga, and S. Tokito, "Printed Strain Sensor with High Sensitivity and Wide Working Range Using a Novel Brittle-Stretchable Conductive Network", *ACS Appl. Mater. Interfaces*, Vol. 12, No. 31, pp. 35282-35290, 2020.

[24] X. Ren, P. K. L. Chan, J. Lu, B. Huang, and D. C. W. Leung, "High dynamic range organic temperature sensor", *Adv. Mater.*, Vol. 25, No. 9, pp. 1291-1295, 2013.

[25] X. Nan, Z. Xu, X. Cao, J. Hao, X. Wang, Q. Duan, G. Wu, L. Hu, Y. Zhao, Z. Yang, and L. Gao, "A Review of Epidermal Flexible Pressure Sensing Arrays", *Biosensors*, Vol. 13, No. 6, pp. 656(1)-656(55), 2023.

[26] J. Lin, R. Fu, X. Zhong, P. Yu, G. Tan, W. Li, H. Zhang, Y. Li, L. Zhou, and C. Ning, "Wearable sensors and devices for real-time cardiovascular disease monitoring", *Cell Rep. Phys. Sci.*, Vol. 2, No. 8, pp. 100541(1)-100541(25), 2021.

[27] H. Wu, Q. Liu, W. Du, C. Li, and G. Shi, "Transparent Polymeric Strain Sensors for Monitoring Vital Signs and beyond", *ACS Appl. Mater. Interfaces.*, Vol. 10, No. 4, pp. 3895-3901, 2018.

[28] C. Wang, J. Zhao, C. Ma, J. Sun, L. Tian, X. Li, F. Li, X. Han, C. Liu, C. Shen, L. Dong, J. Yang, and C. Pan, "Detection of non-joint areas tiny strain and anti-interference voice recognition by micro-cracked metal thin film", *Nano Energy.*, Vol. 34, pp. 578-585, 2017.

[29] C. Berger, R. Phillips, A. Centeno, A. Zurutuza, and A. Vijayaraghavan, "Capacitive pressure sensing with suspended graphene-polymer heterostructure membranes", *Nanoscale*, Vol. 9, No. 44, pp. 17439-17449, 2017.

[30] Q. Zheng, J. hun Lee, X. Shen, X. Chen, and J. K. Kim, "Graphene-based wearable piezoresistive physical sensors", *Mater. Today*, Vol. 36, pp. 158-179, 2020.

[31] Y. Zhao, M. Ren, Y. Shang, J. Li, S. Wang, W. Zhai, G. Zheng, K. Dai, C. Liu, and C. Shen, "Ultra-sensitive and durable strain sensor with sandwich structure and excellent anti-interference ability for wearable electronic skins", *Compos. Sci. Technol.*, Vol. 200, p. 108448, 2020.

[32] J. Lin, R. Fu, X. Zhong, P. Yu, G. Tan, W. Li, H. Zhang, Y. Li, L. Zhou, and C. Ning, "Wearable sensors and devices for real-time cardiovascular disease monitoring", *Cell Rep. Phys. Sci.*, Vol. 2, No. 8, pp. 100541(1)-100541(25), 2021.

[33] Y. Qiao, X. Li, T. Hirtz, G. Deng, Y. Wei, M. Li, S. Ji, Q. Wu, J. Jian, F. Wu, Y. Shen, H. Tian, Y. Yang, and T. L. Ren, "Graphene-based wearable sensors", *Nanoscale*, Vol. 11, No. 41, pp. 18923-18945, 2019.

[34] H. Yu, L. Yu, X. Qi, J. Cui, K. Wu, Y. Liu, L. Chen, and X. Li, "Versatile chewed gum composites with liquid metal for strain sensing, electromagnetic interference shielding and flexible electronics", *J. Mater. Chem. C*, Vol. 11, No. 31, pp. 10455-10463, 2023.

[35] X. Nan, Z. Xu, X. Cao, J. Hao, X. Wang, Q. Duan, G. Wu, L. Hu, Y. Zhao, Z. Yang, and L. Gao, "A Review of Epidermal Flexible Pressure Sensing Arrays", *Biosensors*, Vol. 13, No. 6, pp. 1-55, 2023.

[36] H. Xu, W. Zheng, Y. Wang, D. Xu, N. Zhao, Y. Qin, Y. Yuan, Z. Fan, X. Nan, Q. Duan, W. Wang, Y. Lu, and L. Gao, "Flexible tensile strain-pressure sensor with an off-axis deformation-insensitivity", *Nano Energy*, Vol. 99, p. 107384, 2022.

[37] J. Li, Z. Liao, T. Liang, S. Zhang, B. Tang, X. Fu, G. Li, and Y. Huang, "High sensitivity, fast response and anti-interference crack-based reduced graphene oxide strain sensor for pig acoustic recognition", *Comput. Electron. Agric.*, Vol. 200, p. 107267, 2022.

[38] Z. Zhou, W. Zhang, J. Zhang, Y. Zhang, X. Yin, and B. He, "Flexible and self-adhesive strain sensor based on GNSs/MWCNTs coated stretchable fabric for gesture monitoring and recognition", *Sens. Actuators A Phys.*, Vol. 349, p. 114004, 2023.

[39] H. Yu, L. Yu, X. Qi, J. Cui, K. Wu, Y. Liu, L. Chen, and X. Li, "Versatile chewed gum composites with liquid metal for strain sensing, electromagnetic interference shielding and flexible electronics", *J. Mater. Chem. C*, Vol. 11, No. 31, pp. 10455-10463, 2023.

[40] L. Yang, J. Ma, W. Zhong, Q. Liu, M. Li, W. Wang, Y. Wu, Y. Wang, X. Liu, and D. Wang, "Highly accurate fabric piezoresistive sensor with anti-interference from both high humidity and sweat based on hydrophobic non-fluoride titanium dioxide nanoparticles", *J. Mater. Chem. C*, Vol. 9, No. 15, pp. 5217-5226, 2021.

[41] N. Kang, S. Zhang, F. Tang, J. Wang, and L. Li, "Silver-Hydrogel/PDMS film with high mechanical strength for anti-interference strain sensor", *Colloids. Surf. A Physicochem. Eng. Asp.*, Vol. 654, p. 130071, 2022.

[42] Y. Huang, X. Zeng, W. Wang, X. Guo, C. Hao, W. Pan, P. Liu, C. Liu, Y. Ma, Y. Zhang, and X. Yang, "High-resolution flexible temperature sensor based graphite-filled polyethylene oxide and polyvinylidene fluoride composites for body temperature monitoring", *Sens. Actuators A Phys.*, Vol. 278, pp. 1-10, 2018.

[43] R. Matsuda, S. Mizuguchi, F. Nakamura, T. Endo, Y. Isoda, G. Inamori, and H. Ota, "Highly stretchable sensing array for independent detection of pressure and strain exploiting structural and resistive control", *Sci. Rep.*, Vol. 10, No. 1, p. 12666, 2020.

[44] Y. K. Choi, T. H. Kim, J. H. Song, B. K. Jung, W. Kim, J. H. Bae, H. J. Choi, J. Kwak, J. W. Shim, and S. J. Oh, "Charge transport transition of PEDOT:PSS thin films for temperature-insensitive wearable strain sensors", *Nanoscale*, Vol. 15, No. 17, pp. 7980-7990, 2023.

[45] H. Xu, W. Zheng, Y. Wang, D. Xu, N. Zhao, Y. Qin, Y. Yuan, Z. Fan, X. Nan, Q. Duan, W. Wang, Y. Lu, and L. Gao, "Flexible tensile strain-pressure sensor with an off-axis deformation-insensitivity", *Nano Energy*, Vol. 99, p. 107384, 2022.

[46] Y. Li, R. Wang, G. E. Wang, S. Feng, W. Shi, Y. Cheng, L. Shi, K. Fu, and J. Sun, "Mutually Noninterfering Flexible Pressure-Temperature Dual-Modal Sensors Based on Conductive Metal-Organic Framework for Electronic Skin", *ACS Nano*, Vol. 16, No. 1, pp. 473-484, 2022.

[47] G. Y. Bae, J. T. Han, G. Lee, S. Lee, S. W. Kim, S. Park, J. Kwon, S. Jung, and K. Cho, "Pressure/Temperature Sensing Bimodal Electronic Skin with Stimulus Discriminability and Linear Sensitivity", *Advanced Materials*. Vol. 30, No. 43, pp. 1803388(1)-1803388(9), 2018.

[48] T. Park, H. K. Woo, B. K. Jung, B. Park, J. Bang, W. Kim, S. Jeon, J. Ahn, Y. Lee, Y. M. Lee, T. I. Kim, and S. J. Oh, "Noninterference Wearable Strain Sensor: Near-Zero Temperature Coefficient of Resistance Nanoparticle Arrays with Thermal Expansion and Transport Engineering", *ACS Nano*, Vol. 15, No. 5, pp. 8120-8129, 2021.